ASME Journal of Engineering for Gas Turbines and Power
Online journal at:
https://asmedigitalcollection.asme.org/gasturbinespower

A. Ballotti[1]
Heat Transfer and Combustion Group,
DIEF, Department of Industrial Engineering,
University of Florence,
Via S. Marta 3,
Florence 50139, Italy
e-mail: andrea.ballotti@unifi.it

G. Senatori
Heat Transfer and Combustion Group,
DIEF, Department of Industrial Engineering,
University of Florence,
Via S. Marta 3,
Florence 50139, Italy

S. Galeotti
Heat Transfer and Combustion Group,
DIEF, Department of Industrial Engineering,
University of Florence,
Via S. Marta 3,
Florence 50139, Italy

A. Andreini
Heat Transfer and Combustion Group,
DIEF, Department of Industrial Engineering,
University of Florence,
Via S. Marta 3,
Florence 50139, Italy

Design and Numerical Investigation of a Swirl-Stabilized Hydrogen Burner for Aero Engine Applications

In recent years, the potential of hydrogen as an alternative fuel for the decarbonization of the aeronautical sector has been widely recognized in both scientific and industrial combustion communities. Due to its high reactivity and diffusion, the development of new technologies or the improvement of existing ones to safely and efficiently burn hydrogen, presents significant challenges. Furthermore, nitrogen oxides (NO_x) formation is potentially enhanced, becoming one of the primary factors to address. In this study, a novel 100% hydrogen burner for aero engine applications is designed. The burner realizes a lean, nonpremixed, swirl-stabilized flame achieved with a coaxial triple swirler injector. The innermost channel supplies the fuel, while the two outer channels provide primary and secondary air injections, respectively. The desired injector's flow split and swirl numbers are first individuated exploiting the numerical results from Computational Fluid Dynamics (CFD) Reynolds-averaged Navier–Stokes (RANS) reactive calculations of a parametric simplified geometry, allowing the down-selection of a promising design point. An iterative procedure involving more detailed CFD RANS reactive calculations led to the final geometrical parameters and injector design. The burner is completed with the development of an effusion cooling plate for the dome surface, and validated with a CFD reactive Large Eddy Simulation (LES). The entire workflow is carried out under representative engine operating conditions. Additionally, a detailed LES calculation is performed on a scaled version of the burner operated at ambient pressure, in the perspective of the planned experimental campaign that will take place at Laboratory of Technology for High-Temperature (THT-Lab) of the University of Florence, with results that will be exploited for the test rig design and commissioning.
[DOI: 10.1115/1.4069547]

Keywords: design, hydrogen, burner, numerical combustion, aero engines

1 Introduction

The focus of the scientific and industrial combustion communities on alternative synthetic fuels has significantly increased over recent years. This is primarily due to a series of regulatory measures, both European and international, with the objective of achieving net-zero CO_2 emissions by 2050, making hydrogen one of the key players in the energy transition for engines and gas turbines [1]. However, it is essential that hydrogen production technologies meet environmental requirements to avoid nullifying the advantages of its utilization as a carbon-free fuel [2].

The different characteristics of hydrogen introduce several new challenges from a design perspective and in terms of the combustor operability. For instance, the elevated flame temperatures associated with hydrogen combustion, compared to conventional fuels, can lead to an increase in NO_x emissions. This aspect can be mitigated through temperature control by operating under leaner conditions, thanks to its higher reactivity and wider flammability range. Furthermore, the high flame propagation speed makes the mixture more prone to flashback in premixed systems [3] and its higher diffusivity alters the internal flame structure, affecting its composition and potentially leading to the onset of combustion instabilities.

Focusing on the aeronautical sector, additional challenges arise due to the variety of conditions under which the combustor must safely operate, ensuring a stable and efficient flame during each phase of flight while adhering to emission limits on pollutants for certification. However, the development of novel hydrogen combustion technologies for aero engines is essential to reduce the carbon footprint and achieve meaningful progress toward decarbonizing the aerospace sector. While the challenge is far from simple, it is one that must be addressed with urgency and innovation.

For these reasons, in recent years, several initiatives have emerged to promote the development and study of hydrogen combustion technologies specifically for aircraft engines. For instance, the primary goal of the HYdrogen DEmonstrator for Aviation (HYDEA) project is to develop a hydrogen propulsion system for a zero-CO_2 low-emissions aircraft by 2035 [4].

Turbo Expo: Turbomachinery Technical Conference & Exposition (GT2025), June 16–20, 2025. GT2025.
[1]Corresponding author.
Manuscript received July 9, 2025; final manuscript received July 28, 2025; published online October 6, 2025. Editor: Jerzy T. Sawicki.

Supported by an international consortium, this initiative aims to demonstrate the feasibility of hydrogen propulsion while tackling critical technological and emission-related challenges.

The HydrogEn combuSTion In Aero engines (HESTIA) project, coordinated by Safran, involves several partners including the University of Florence, with the common aim of enhancing the scientific understanding of the hydrogen combustion process using numerical and experimental methodologies [5].

In this work, a novel nonpremixed swirl-stabilized 100% hydrogen lean burner for aero engine application is designed under representative engine conditions. Even though different technologies are available, swirl-stabilized burners ensure a fast fuel-air mixing rate, which can be adjusted by controlling the amount of swirl, and produce compact flames with high power density [6], a crucial requirement for aero engines.

After a burner conceptualization, the early design phase exploits simplified Computational Fluid Dynamics (CFD) Reynolds-averaged Navier–Stokes (RANS) calculations to investigate the impact of the injector's degrees of freedom on typical parameters, in order to down-select a promising configuration to be taken as a reference for the subsequent design phases.

Then, a more detailed parametric fluid geometry is realized and its degrees of freedom are iteratively calibrated through CFD RANS calculations to fit the down-selected configuration. An effusion cooling system for the combustor's dome surface is introduced and tested in both co-rotating and counter-rotating configurations with respect to the tangential components of the swirlers. The design phase is described in Sec. 2.

The geometry, consisting of the upstream plenum, the final part of the fuel line, the burner, the dome's effusion cooling system, and the flame tube is subsequently tested with a detailed reactive Large Eddy Simulation (LES) calculation under representative engine conditions. The numerical setup and the results of this calculation are presented in Sec. 3.

In the perspective of the planned experimental campaign that will take place at Laboratory of Technology for High-Temperature (THT-Lab) of the University of Florence, the design previously carried out is geometrically scaled to adapt to the existing reactive test cell, and numerically investigated under ambient pressure and preheated air conditions with a reactive LES calculation. The burner's scaling, the numerical setup, as well as the results coming from this analysis, which will be exploited for the test rig design and commissioning, are presented in Sec. 4.

Finally, the conclusions are summarized in Sec. 5.

2 Design of a Novel Burner

A representative thermodynamic cycle and the design conditions are defined after identifying an appropriate application range for the burner. The design conditions consist of the reference pressure P_3^{ref}, the pressure drop across the burner ΔP^{ref}, the air and fuel temperatures T_3^{ref}, T_f^{ref}, and the air and fuel mass flow rates $W_{\mathrm{sw}}^{\mathrm{ref}}$, W_f^{ref} supplying the burner leading to a reference swirlers' equivalence ratio $\Phi_{\mathrm{sw}}^{\mathrm{ref}} = 0.8$.

The flame stabilization strategy relies on a novel triple swirler coaxial injector, with the innermost channel supplying a swirled hydrogen stream, and the two outer channels providing a primary and secondary swirled air injections, respectively.

The numerical design workflow is essentially made up of three different phases: design space exploration, fluid geometry calibration, and finalization of the geometry. Each phase is explained in a dedicated subsection.

2.1 Design Space Exploration. In the design space exploration phase, the objective is to analyze a design space of potential candidates in a reduced amount of time and with reduced computational efforts.

2.1.1 Preprocessing. A parametric simplified geometry is created in ANSYS Design Modeler, consisting of a 1 deg slice of a cylindrical flame tube, assuming a perfectly azimuthal periodicity. The inlet sections of fuel and oxidizer are realized with numerical patches lying on the same plane of the combustor dome, meaning that explicit geometries for the three swirlers are not considered during this phase. The numerical patches are parametrically defined by varying minimum and maximum radii which are calculated based on characteristic bulk velocities of the incoming flow while modifying the flow split between the primary and secondary air injections.

To define the effective area for fuel injection, the laminar flame speed s_L^{ref} of a one-dimensional, unstretched premixed freely propagating flame is calculated in Cantera [7] considering a mixture with equivalence ratio $\Phi_{\mathrm{sw}}^{\mathrm{ref}}$, pressure $P_3^{\mathrm{ref}} - \Delta P^{\mathrm{ref}}$, a temperature resulting from the perfect mixing of oxidizer and fuel at temperatures T_3^{ref} and T_f^{ref}, respectively. The chemical kinetics relies on the detailed reaction mechanism of O'Conaire [8] accounting for 11 species and 19 reactions. A reference bulk velocity $V_{\mathrm{H_2}}^{\mathrm{ref}}$ is chosen as a multiple of the laminar flame speed of the mixture

$$V_{\mathrm{H_2}}^{\mathrm{ref}} := C\, s_L^{\mathrm{ref}} \tag{1}$$

The effective area to consider for fuel injection is then calculated from the fuel mass flowrate W_f^{ref} and the hydrogen bulk velocity $V_{\mathrm{H_2}}^{\mathrm{ref}}$. The requirement for the constant $C \geq 1$ is to guarantee a safe compensation of the turbulent flame speed and the positive contribution of the stretch on the consumption speed.

In this early preliminary phase, the reference lean lifted flame [9] developed at IMFT is considered, assuming the same ratio between hydrogen bulk velocity and laminar flame speed. This choice brings with it some limitations, since the operating conditions and equivalence ratio differ between [9] and the current configuration, meaning that the response of both turbulence and stretch on the flame speed can be different. At the same time, a perfect alignment between effective and geometric areas is assumed in this preliminary phase, while at more mature stages of the design described in Secs. 2.2 and 2.3, the burner is explicitly resolved retaining the geometric areas found in the design exploration. A subunitary discharge coefficient, defined as the ratio between the effective and geometric areas $C_D = A_{\mathrm{eff}}/A_{\mathrm{geo}}$, further increases the bulk velocity due to a reduction of the effective area and modifies the ratio between velocity $V_{\mathrm{H_2}}^{\mathrm{ref}}$ and s_L^{ref} in the direction of considering a higher flame response to stretch and turbulence.

To consider the possibility of a multiperforated geometry for the fuel injection, as well as the possibility of a strong recirculation inducing a central flow blockage in case of a constant section duct [10], the area for fuel injection results by the sum of the effective injector's area and an additional area for the solid or for the blocked flow. The output of these considerations is a geometrical, circumferential area on the available surface, leading to a maximum radius for the fuel injector patch. Assuming a constant solid thickness of the burner, a minimum radius for the outer coaxial air injections is then available.

Regarding the determination of the radii for the air inlet patches, the total effective area is calculated from $W_{\mathrm{sw}}^{\mathrm{ref}}$ and a reference bulk velocity $V_{3,1}^{\mathrm{ref}}$ in turn determined as

$$V_{3,1}^{\mathrm{ref}} = \sqrt{2\Delta P^{\mathrm{ref}}/\rho_3^{\mathrm{ref}}} \tag{2}$$

with ρ_3^{ref} a reference air density calculated from the ideal gas law considering P_3^{ref} and T_3^{ref}. Once available the total effective area, a minimum exit radius, a constant solid thickness, and assuming a flow split between the primary and secondary air streams, it is possible in turn to define their minimum and maximum radii from simple geometrical considerations.

The parametric geometry, as well as the imposed boundary conditions, are presented in Fig. 1. Since the visualization of 1 deg slice makes interpretation difficult, a representative 20 deg slice is reported in the figure only for visualization purposes. The velocity inlet conditions are imposed in a cylindrical reference frame

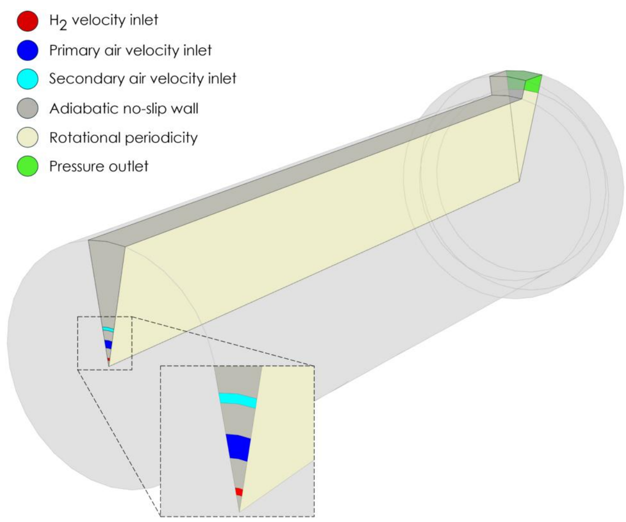

Fig. 1 Simulacrum of combustor slice used in the design exploration phase with the assigned boundary conditions

Table 1 Summary of the degrees of freedom

Degree of freedom	R	γ_{H_2}	γ_1	γ_2
Definition	$\dfrac{A^1}{A^1+A^2}$	$\tan^{-1}\left(\dfrac{V_\phi^{H_2}}{V_z^{H_2}}\right)$	$\tan^{-1}\left(\dfrac{V_\phi^1}{V_z^1}\right)$	$\tan^{-1}\left(\dfrac{V_\phi^2}{V_z^2}\right)$

$$\begin{cases} V_z^K = \dfrac{W^K}{\rho^K A^K} \\ V_r^K = 0 \\ V_\phi^K = \tan(\gamma_K) V_z^K, \quad K \in \{H_2, 1, 2\} \end{cases} \tag{3}$$

where index K refers to the fuel injection, the primary air injection, or the secondary air injection, respectively, while z, r, and ϕ refer to the axial, radial, and tangential components.

All the walls are considered as adiabatic, no-slip walls, and a pressure $P_3^{\text{ref}} - \Delta P^{\text{ref}}$ is imposed at the outlet section. In virtue of the geometrical assumptions made, rotationally periodic conditions are imposed on the lateral surfaces.

Four different degrees of freedom, actively controlling the creation of the parametric geometry and the computational setup, are individuated: the area ratio R, controlling the flow split between the two air streams and defined as the ratio between the area of the primary air injection and the total air injection area, and the tangential angles γ_K for each injection, leading to an incoming swirled flow inside the flame tube. To limit the number of degrees of freedom, null radial injection angles are assumed. However, the impact of nonperfectly orthogonal ducts is considered in the later stages, leading to the configuration presented in Sec. 2.3. The chosen degrees of freedom are summarized in Table 1 and their graphical representation is provided in Fig. 2.

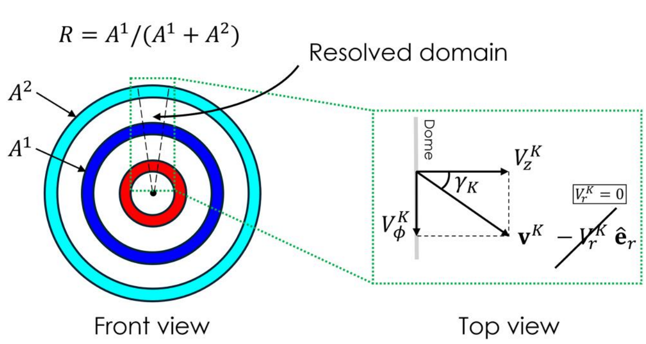

Fig. 2 Graphical representation of the explored degrees of freedom

The parametric geometry is discretized with a tetrahedral mesh constituted of roughly 100 thousands elements majorly concentrated around the injection locations. Even with a similar order of magnitude, the exact number of cells depends on the specific configuration and on the radial extension and location of the inlet patches.

All the numerical calculations are conducted looking for steady-state solutions adopting the pressure-based formulation of the commercial CFD finite volumes solver ANSYS Fluent 2023 R1, with a RANS realizable $k-\varepsilon$ turbulence model with scalable wall functions. To handle turbulent combustion, the flamelet generated manifold (FGM) model [11] in its finite rate closure formulation is chosen exploiting diffusive flamelets. The chemical kinetics relies on the O'Conaire detailed mechanism [8], and the unburnt properties and thermal conductivity of the mixture are calculated in Cantera and imported in the solver through polynomials. The progress variable c is defined as

$$c := Y_{H_2O} + 10\, Y_{HO_2} \tag{4}$$

The choice of some objective functions is required to close the problem: to ensure a sufficient durability of the burner's components, the temperatures on the metal surfaces must be limited. Furthermore, the NO_x emissions are a primary factor to address. For these reasons, premising that the simulations performed do not include neither conjugate heat transfer analyses nor heat loss phenomena, the chosen objective functions are the mean dome temperature $T_{\text{Dome}}^{\text{Mean}}$, the maximum dome temperature $T_{\text{Dome}}^{\text{Max}}$, and the NO_x emissions. All the objective functions are output parameters of the numerical calculations. Additionally, other quantities of interest are monitored in CFD calculations, like the extension of the central recirculation zone permitting to distinguish between jet and swirl-stabilized flame configurations. The last step of the preprocessing phase consists of the definition of proper lower and upper bounds for the degrees of freedom to define the design space.

2.1.2 Results and Postprocessing. The calculations are executed in parallel on the high performance computing cluster of the University of Florence, and results are collected in a table used to carry out continuous response surfaces describing the sensitivity of the objective functions with respect to the degrees of freedom. Before the response surfaces creation, the following normalization is performed:

$$\overline{Q} := \frac{Q - Q^{\text{Min}}}{Q^{\text{Max}} - Q^{\text{Min}}} \tag{5}$$

where Q is the generic quantity belonging to the degrees of freedom or to the objective functions, Q^{Max} and Q^{Min} are its maximum and minimum values assumed in the table, respectively, and $\overline{Q}$ is the normalized, nondimensional quantity.

Figure 3 shows the response surface of $\overline{T_{\text{Dome}}^{\text{Mean}}}$. The global maximum is achieved at the highest tangential angles across all three swirlers, with a flow split unbalancing the mass flow rate on the secondary air stream ($\overline{R} = 0$). A local maximum gradually shifts toward higher values of $\overline{\gamma_1}$ and $\overline{\gamma_2}$ for increasing values of $\overline{\gamma_{H_2}}$, eventually becoming the global maximum.

At intermediate values of $\overline{R}$, temperatures remain relatively high, and the global maximum shifts toward lower values of $\overline{\gamma_1}$ and $\overline{\gamma_2}$ for increasing values of $\overline{\gamma_{H_2}}$. Finally, with a flow split predominantly favoring the primary injection ($\overline{R} = 1$), lower temperatures are generally observed, that rise significantly at high values of $\overline{\gamma_{H_2}}$. The local minimum of the mean dome temperature is reached for intermediate values of $\overline{\gamma_{H_2}}$ and $\overline{\gamma_1}$, at the highest value of $\overline{\gamma_2}$. The

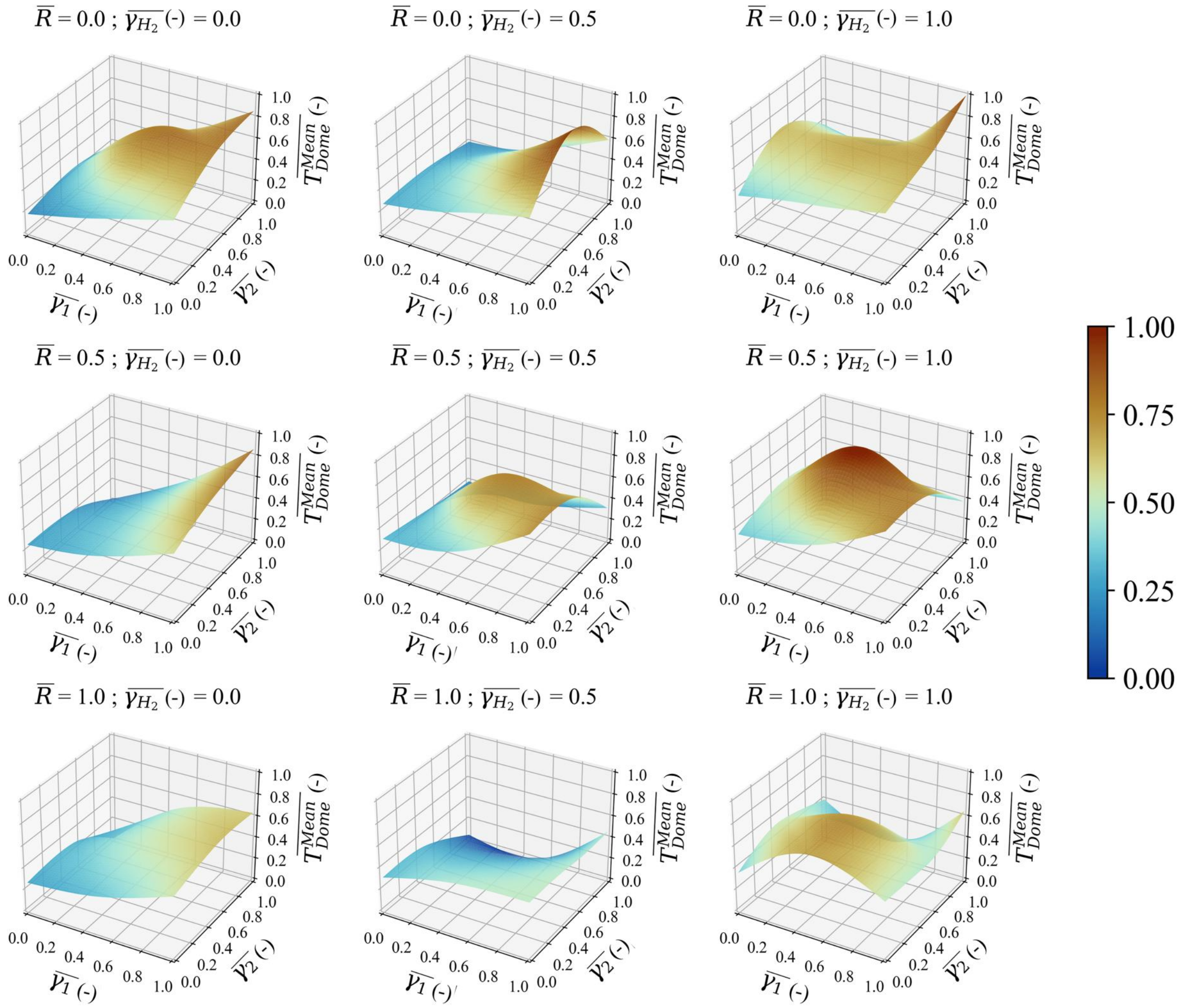

Fig. 3 Visualization of the obtained 4D response surface for the normalized mean dome temperature

response surface provided by the normalized maximum dome temperature $\overline{T^{\mathrm{Max}}_{\mathrm{Dome}}}$ is not reported as it shows the same trends, meaning that higher temperature peaks are not associated with the presence of hot spots on the dome surface.

Figure 4 shows the response surface of the normalized NO_x emissions. In all cases, the minimum NO_x levels are observed at the lowest values of $\overline{\gamma_1}$ and $\overline{\gamma_2}$. A thorough inspection of these configurations reveals jet flames characterized by shorter residence times inside the flame tube. For low $\overline{\gamma_1}$ and $\bar{R}$ values, NO_x emissions show an almost monotonic dependence on $\overline{\gamma_2}$. This dependence is lost for higher values of $\overline{\gamma_1}$, where a local maximum appears. In presence of a balanced flow split, the NO_x emissions show the same behavior for increasing values of both $\overline{\gamma_1}$ and $\overline{\gamma_2}$, at all $\overline{\gamma_{\mathrm{H_2}}}$ values. Finally, at $\bar{R} = 1$ the emissions generally increase together with $\overline{\gamma_2}$ except for intermediate values of $\overline{\gamma_{\mathrm{H_2}}}$ and $\overline{\gamma_1}$ where a trend reversal is observed at high values of $\overline{\gamma_2}$.

The landscape provided by the design space exploration reveals that the explored range of the degrees of freedom can realize both jet and swirl-stabilized flames. The former typically occur for low tangential angles imposed on the primary and secondary air streams, resulting in reduced NO_x emissions due to shorter residence times within the flame tube. The latter, as expected, are achieved for higher tangential angles of the injection streams. All calculated flames stabilize anchored to the fuel injector along the stoichiometric isolines. Recalling that the goal of the exploration is to identify a design point characterized by a swirl-stabilized flame minimizing as possible both gas temperatures on the surfaces and NO_x emissions, a promising design point is characterized by the highest $\bar{R}$ and $\overline{\gamma_2}$, with intermediate values of $\overline{\gamma_{\mathrm{H_2}}}$ and $\overline{\gamma_1}$.

Figure 5 shows the normalized axial velocity, equivalence ratio, static temperature, and product formation rate distributions on the *YZ* plane of the down-selected candidate. The central recirculation zone extends from the beginning to the end of the computational domain, while an external recirculation zone appears at the intersection between the dome and the flame tube's liner. Low-velocity zones are visible around the lips separating the fuel and the oxidizer injections. The combination of these low-velocity zones with the position of the isoline at stoichiometric composition can be responsible of the flame anchoring, as discussed in Refs. [12] and [13]. A strong temperature difference is observed between the exhaust gases in the central recirculation zone and the ones recirculating externally.

2.2 Fluid Geometry Calibration. The previous simplified stage is useful to identify a swirl-stabilized configuration minimizing the gas temperature distribution on the dome surface and the NO_x emissions. In order to explicitly design the swirlers, the previous inlet surfaces are considered downstream sections of the swirled coaxial ducts, and the degrees of freedom regulating the tangential angles of the three injections are converted into useful parameters.

One of the immediately available quantities from the previous analysis is the swirl number, defined as

$$S_K := \frac{\int_{A^K} (rV_\phi)\rho\mathbf{v}\cdot\hat{\mathbf{n}}\,dA}{r_K^{\mathrm{Max}}\int_{A^K}(V_z)\rho\mathbf{v}\cdot\hat{\mathbf{n}}\,dA}, \quad K\in\{\mathrm{H_2},1,2\} \tag{6}$$

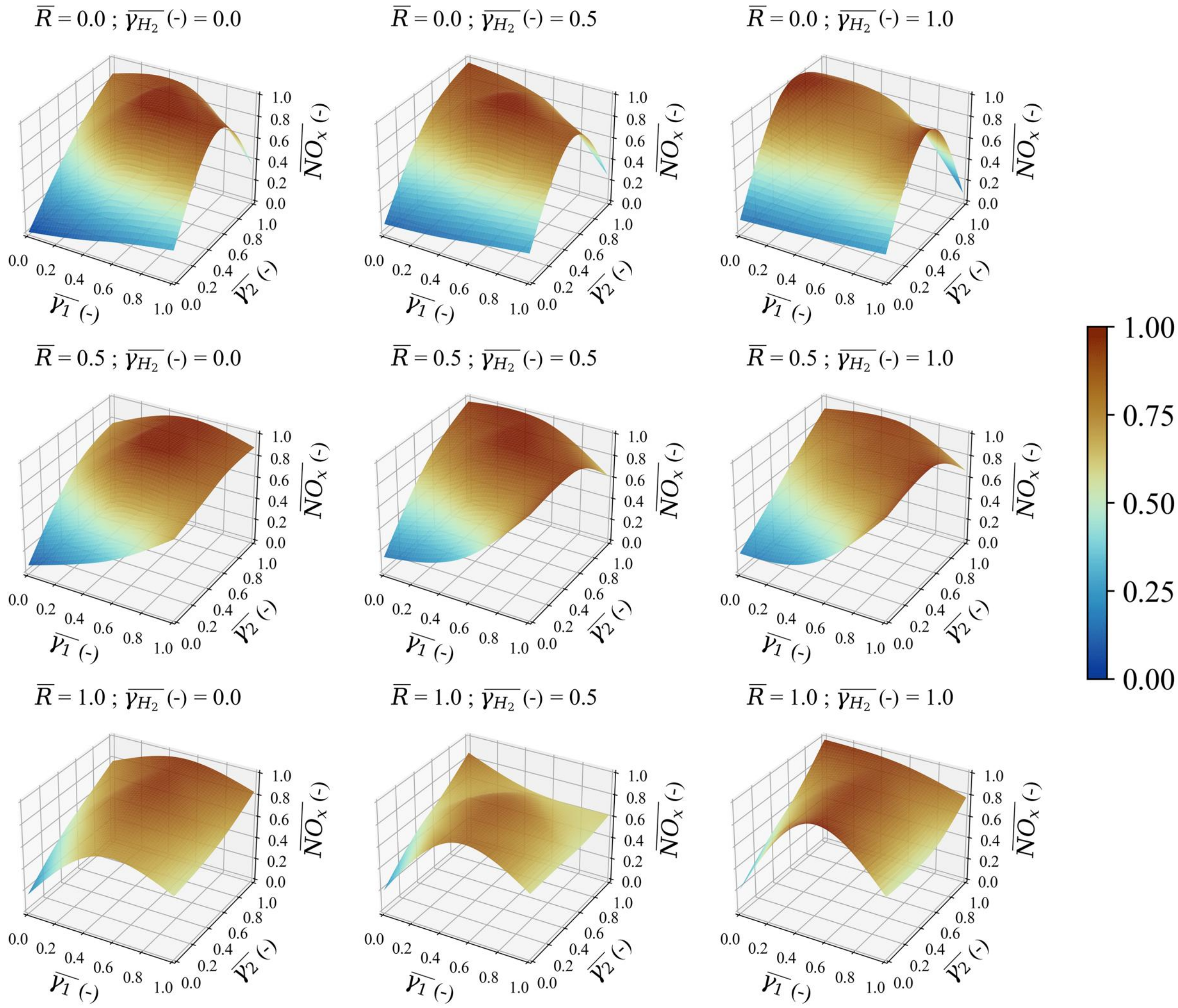

Fig. 4 Visualization of the obtained 4D response surface for the normalized NO_x emissions

where $\mathbf{v} = V_z\,\hat{\mathbf{e}}_z + V_\phi\,\hat{\mathbf{e}}_\phi + V_r\,\hat{\mathbf{e}}_r$ is the velocity, r is the radial coordinate, $\hat{\mathbf{n}}$ is the unitary vector identifying the pointing out normal, and r_K^{Max} is the maximum radial coordinate on the integration surface A^K.

Applying Eq. (6) to the down-selected design point, the swirl numbers $S_{\mathrm{H_2}}^{\mathrm{ref}} = 0.72$, $S_1^{\mathrm{ref}} = 0.72$, and $S_2^{\mathrm{ref}} = 0.80$ are obtained. Although they are used as reference values for the swirlers' design, deviations from these values are still permitted at this stage.

2.2.1 Air Swirlers Calibration. A parametric 3D geometry is obtained by performing a 360 deg revolution of the design space exploration geometry, providing the flame tube and the exit sections of the injections. Initially, the fluid patch of the fuel stream is maintained, while for the two air channels a radial swirler configuration is conceptualized. A common solid flat vane is designed and tangentially repeated obtaining a pattern accounting for 24 vanes exploited to create the fluid swirling ducts upstream the flame tube. A plenum is positioned upstream the swirling ducts, supplying the air swirlers and completing the parametric geometry that is represented in Fig. 6. The geometric area of the fluid section in the swirling ducts is maintained higher than the geometric exit section of the burner, where the reference section lies. The considered degrees of freedom controlling the parametric geometry are the radial angles of the inclined vanes α_1, α_2, and the geometric areas of the exit sections (or, equivalently, their discharge coefficient C_D which is assumed unique for the two streams), that are calibrated to obtain the desired swirl numbers and the design pressure drop across the burner. The chosen parameters are anyway not independent. Indeed, when the inclination of the blades modifies, also the pressure drop across the burner is affected due to a change in the tangential component of the velocity, but not in the axial one (assuming minimum density variations), resulting in a different acceleration of the flow across the swirler. On the other side, modifying the geometric area of the exit section of the swirling ducts results in a modification of the axial velocity which in turn

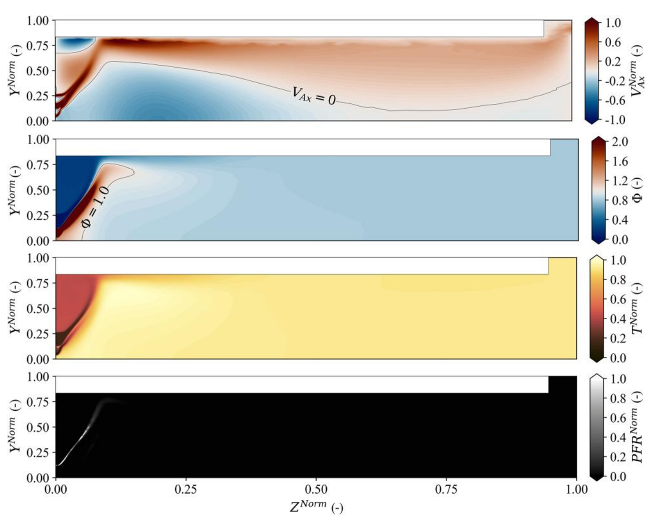

Fig. 5 Normalized axial velocity, equivalence ratio, static temperature, and product formation rate of the down-selected design point

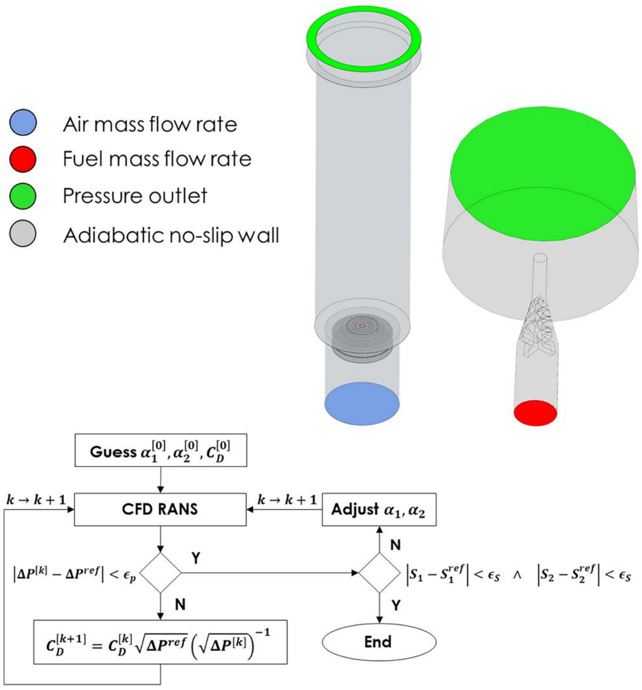

Fig. 6 Geometries adopted for the air swirlers (top left) and fuel swirler (top right) calibrations, with the assigned boundary conditions. Flowchart of the iterative procedure used for the air swirlers calibration (bottom).

modifies the swirl numbers according to Eq. (6). To properly calibrate the geometry, the iterative procedure reported in Fig. 6 is applied. The iteration formula, derived from the isentropic relationship in Eq. (2), expresses the ratio between the real discharge coefficient and its current approximation at iteration k as the ratio between the square roots of the reference and current pressure drops, providing an estimation of the real discharge coefficient. No physical relationships are instead considered to adjust the angles α_1 and α_2, which are calibrated progressively modifying the vanes' inclination with a constant step of $\Delta\alpha = 0.5$ deg. The procedure exploits the same CFD solver and numerical setup used during the design exploration phase, and terminates when the convergence criteria provided by tolerances ε_p and ε_s are both reached.

2.2.2 Fuel Swirler Calibration. A convergent, helical, axial swirler is conceptualized and calibrated to realize the swirling fuel duct. The helical convergent shape ensures a very fast fuel flow entering the combustion chamber through a final section geometrically sized from Eq. (1), while limiting the swirl number drop caused by the axial flow acceleration. The upstream diameter of the convergent duct is based on typical diameters of fuel lines on academic burners. A simplified 3D parametric geometry is exploited considering the helical axial pitch as unique degree of freedom defining the tangential component imposed to the velocity, and the desired swirl number S_{H_2} as objective function. The geometry consists of the fuel line entering a cylindrical plenum with the same radius of the reference flame tube, and the assigned boundary conditions are the hydrogen mass flowrate W_f^{ref} at the inlet, and the pressure $P_3^{\mathrm{ref}} - \Delta P^{\mathrm{ref}}$ at the outlet.

The geometry used for the calibration of the fuel swirler is shown on the right side of Fig. 6, along with the assigned boundary conditions. Figure 7 instead provides a sketch of the component, also indicating the axial pitch and the location where the swirl number is evaluated.

2.3 Finalization of the Geometry.

The two fluid geometries obtained for the calibrated air and fuel swirling ducts are subsequently combined. To reduce the dimension of the lips separating the injections, while enhancing the strain levels of the flow field where the air and the fuel start mixing, a radially

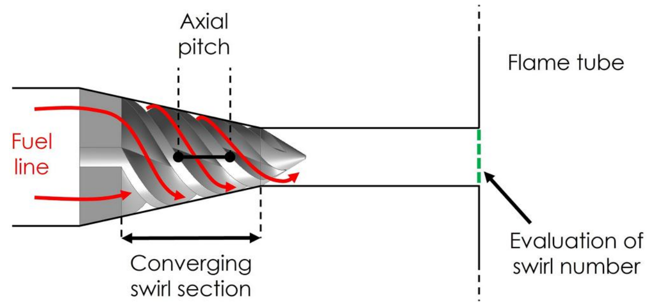

Fig. 7 Sketch of the fuel swirler. The helical axial pitch, used as a degree-of-freedom, is reported along with the location where the swirl number is numerically evaluated.

convergent path is imposed on the final sections of the primary and secondary air swirlers. The combustion chamber is realized keeping the flame tube obtained from the 360 deg revolution of the design exploration geometry, and modifying the outlet section with a convergent nozzle to prevent numerical backflow. Effusion cooling is implemented on the dome surface to limit the dome temperature for safe burner operation. Indeed, when transitioning to a detailed 3D computation, it becomes possible and deemed useful to also consider the realistic scenario of cooling injection. A simplified effusion cooling configuration is chosen, with cylindrical holes arranged on four equally radially spaced rings, with a tangential pitch around seven hole's diameters. The cooling air mass flow rate $W_{\mathrm{cool}}^{\mathrm{ref}}$ is derived from a defined flow split between cooling and combustion air, with known total air mass flow rate W_3^{ref}. Assuming a certain discharge coefficient, the holes' geometric area can be retrieved, with a total of 90 effusion cooling holes. In the computation, the effusion holes are implemented with patches located on the dome, avoiding to explicitly create the cylindrical holes. This potentially allows to numerically test the cooling system with both co-rotating and counter-rotating tangential directions with respect to the swirlers, without modifying the model geometry. The direction of the cooling injection on each hole patch is defined by

$$\mathbf{d} := \sin(\theta_z)\,\hat{\mathbf{e}}_z + \cos(\theta_z)\sin(\theta_r)\,\hat{\mathbf{e}}_r \pm \cos(\theta_z)\cos(\theta_r)\,\hat{\mathbf{e}}_\phi \tag{7}$$

with θ_z and $\theta_r = 0$ deg expressing the impact angle of the effusion holes with respect to the dome surface and the compound angle quantifying the radial deviation with respect to a purely axial–tangential injection, respectively. The choice of the sign of the last term is the kernel of the co-rotating and counter-rotating tangential directions imposed to the effusion cooling system in the numerical simulations.

A strong impact of the tangential direction of the effusion cooling path is observed and illustrated in Fig. 8. Indeed, a complete alteration of the shape and dimensions of the recirculation zones and the temperature distribution in the case of the co-rotating path is observed, while the flow field is preserved and the temperatures in the outer recirculation zone are lowered in the case of the counter-rotating path. This phenomenon can possibly be explained by the competition between the low-pressure zones on the dome surface created by the

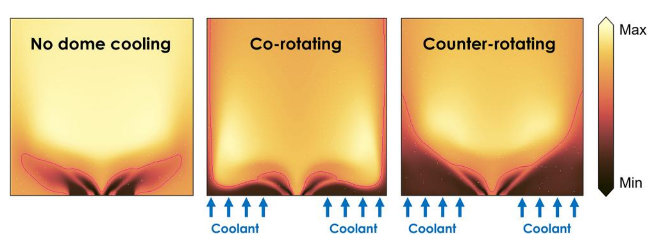

Fig. 8 Effect of the tangential direction of the effusion cooling path on the static temperature field. The solid line indicates the same temperature isosurface.

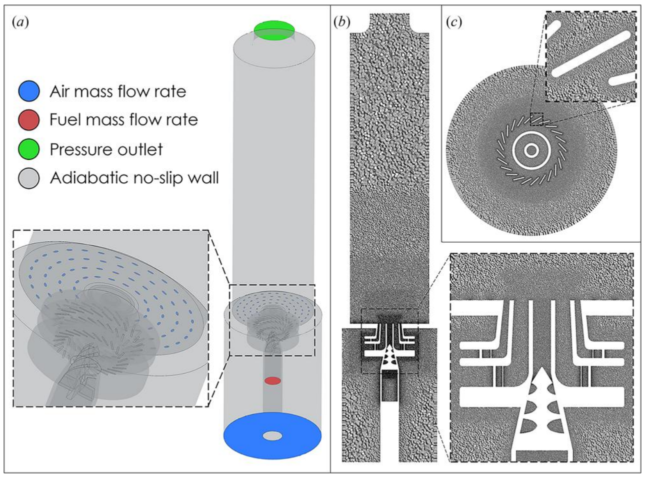

Fig. 9 Computational domain with the assigned boundary conditions (*a*). Polyhedral mesh adopted for the LES calculation and refinement in the swirling ducts region (*b*). Mesh detail on a plane transversal to the secondary air swirler vanes (*c*).

high-velocity injections of the coolant, and the global swirl number of the system [10], increasing with the co-rotating effusion cooling path and decreasing with the counter-rotating one.

While in the first case the two effects add up, leading to a complete radial spread of the oxidizer injections, in the second one they cancel each other. The counter-rotating configuration is finally chosen for the effusion cooling system.

3 Numerical Results Under Representative Engine Conditions

The obtained final geometry of the burner is validated with a LES calculation under high-pressure conditions exploiting the pressure-based formulation of ANSYS Fluent 2023 R1. The domain is discretized with a static polyhedral mesh accounting for 40 million cells.

The complete geometry and the numerical mesh are shown in Fig. 9. Local refinements are applied from the swirled ducts to the beginning of the flame tube to properly resolve the first mixing zone and avoid losing any turbulent structure generated from the swirlers. The same strategy is applied to the fluid portion confined between the swirlers' vanes, where a minimum of 30 cells between surface–surface and edge–edge gaps is ensured. The subgrid scale closure for the momentum relies on the Smagorinsky–Lilly model with dynamic stresses [14–16]. The pressure–velocity coupling is managed by the SIMPLEC algorithm, and the simulation is executed adopting a bounded second-order implicit scheme for time advancement with a constant time step size of 1×10^{-6} s. Turbulent combustion is solved with the finite rate FGM model, together with the stretch correction by Klarmann [17,18] to account for the stretch effects.

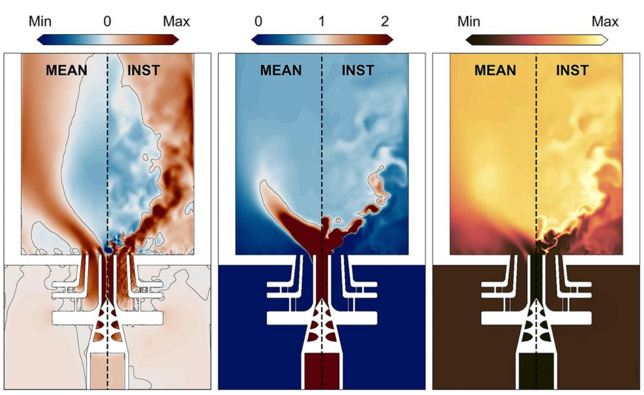

Fig. 10 Mean and instantaneous distributions of axial velocity (left), equivalence ratio (center), and static temperature (right) on a portion of the *YZ* plane. The solid lines highlight the null axial velocity isosurface (left) and the isosurface at stoichiometric composition (center).

Figure 10 shows the mean (left) and instantaneous (right) distributions of the axial velocity, equivalence ratio, and static temperature. It can be observed the presence of a high-intensity central recirculation zone in the proximity of the exit of the fuel injector. A similar behavior is observed in previous works [12] when a high swirl number in the fuel line combines with the absence of axial recess of the fuel injection, and in Refs. [10] and [12], it is argued that this high-intensity recirculation can produce a flow blockage on the fuel line leading to a strong fuel radial acceleration. This phenomenon could enhance the strain of the velocity field in the proximity of the lips separating fuel and primary air injections and could move the stoichiometric line away from this surface. As a result, this could lead to a richer mixture surrounding the primary injector lip and to higher stretch levels in its proximity, making the flame anchoring on the injector more difficult. However, these conditions are not sufficient for the current configuration since the flame anchoring on the injector is observed, as can be noticed from the temperature distribution in Fig. 10. Indeed, the heat release is concentrated on a flame front located on the stoichiometric isoline oscillating inside the final section of the internal surface of the primary air channel. A secondary flame front appears downstream the first one, providing to the flame a typical M-shape. A recirculation zone at the end of the fuel swirler is observed, partially extending along the fuel channel and occasionally combining with the central recirculation zone inside the combustion chamber. Due to the nonpremixed injection, and since an increase of the fresh fuel temperature is not observed, this recirculation does not lead to particular issues under the investigated operating conditions.

The top left and top right contour plots reported in Fig. 11 show the mean and instantaneous distributions of the velocity magnitude extracted on transversal planes with respect to the primary and secondary swirlers' vanes, respectively. The flow separation at the trailing edge of the vanes promotes the formation of turbulent structures convected to the combustion chamber. The acceleration produced by the flow passage between the swirlers' vanes is clearly visible, together with a second strong acceleration occurring in the innermost zone of the air channels due to a reduced section downstream the planes. The innermost zone corresponds to the fuel stream which is characterized by a higher velocity with respect to the air channels.

The bottom plot of Fig. 11 shows the performance of the dome's effusion cooling system in terms of the mean and instantaneous distributions of gas temperature extracted on the hot side of the dome surface. The innermost and outermost zones of the dome are invested by gas at a lower temperature with respect to the rest of the surface. For the outermost zone, this is due to an instantaneous colder gas distribution at any time, whereas for the innermost one it can be observed a tangential alternation of cold and hot spots caused by the presence of the secondary air injection and hot gas pockets recirculating inside the combustion chamber. This is also observed at higher radial coordinates, where the influence of the secondary air injection reduces, and higher mean temperatures are reached.

4 Burner Scaling for Ambient Pressure Test Rig

The reference thermodynamic cycle is scaled to conditions achievable in the reactive test rig installed at THT-Lab of the University of Florence. Tests will be performed in a single sector chamber enclosed in an outer vessel, with optical access on the flame. In particular, the combustion chamber of the rig is composed of a 186 mm long flame tube with close-to-square cross section, with 74×72 mm edges. This is followed downstream by a transition zone converting the rectangular cross section to a circular one, which continues with a 206 mm long cylindrical part with diameter of 102 mm. In the test rig, after the cylindrical duct, the combustion

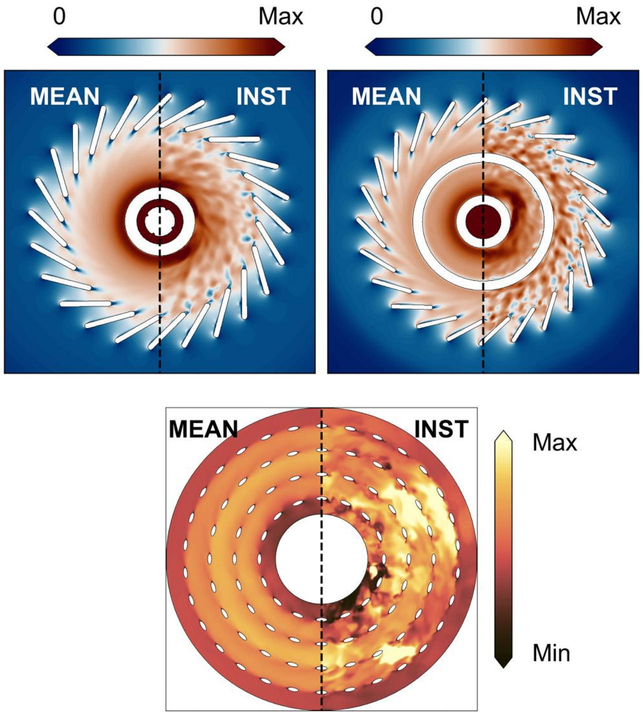

Fig. 11 Mean and instantaneous distributions of velocity magnitude on planes transversal to the primary (top left) and secondary (top right) air swirler vanes. Mean and instantaneous distribution of gas temperature on the dome surface (bottom).

chamber exhaust mix with cooling air flowing in the annular space between the liner and the confining vessel, bypassing the combustion process. Test campaign will be performed at ambient pressure, therefore it is necessary to scale the burner operating conditions. Due to the different dimensions between the flame tube used for high-pressure numerical simulations, and the flame tube of the atmospheric reactive test cell, the burner needs to be geometrically scaled, together with the reactants' mass flow rates. The scaling of the thermodynamic cycle is operated preserving the flow function

$$\begin{cases} W_{\mathrm{sw}}^{\mathrm{Lab}} = Q\, W_{\mathrm{sw}}^{\mathrm{ref}} \dfrac{P_3^{\mathrm{Lab}}}{P_3^{\mathrm{ref}}} \sqrt{\dfrac{T_3^{\mathrm{ref}}}{T_3^{\mathrm{Lab}}}} \\ \Phi_{\mathrm{sw}}^{\mathrm{Lab}} = \Phi_{\mathrm{sw}}^{\mathrm{ref}} \end{cases} \tag{8}$$

where $W_{\mathrm{sw}}^{\mathrm{Lab}}$, P_3^{Lab}, T_3^{Lab} are the swirlers' air mass flow rate, a presumed reference pressure upstream the burner obtained assuming the same percentage pressure drop from the high-pressure design, and the fresh air temperature considered for the atmospheric test cell, respectively. The equivalence ratio $\Phi_{\mathrm{sw}}^{\mathrm{Lab}}$ solely accounts for the air contribution to supply the swirlers, while Q is a quadratic scaling factor defined as the ratio between the cross-sectional areas of the flame tube in the test cell and the one considered in Sec. 3 for high-pressure conditions. While the geometric areas of the burner are scaled by a factor Q, it is important to specify that not all dimensions are scaled with this law. Indeed, the solid thickness of the swirlers has to respect the constraints imposed by manufacturing. At the same time, the lip thickness has to remain limited to avoid large recirculating zones downstream the injector lips. Furthermore, the fuel line's diameter upstream the convergent helical swirler has to respect the dimensions of the existing infrastructure at THT-Lab, meaning that the ratio between the radii downstream (scaled with factor $\sqrt{Q}$) and upstream the fuel swirler, is not maintained, producing a different flow axial acceleration along the fuel stream. Since the hydrogen injector's swirl number is a necessary condition to lift hydrogen-air flames [19], in this case, the decision is to adjust the value of the helical axial pitch to retain as possible the design swirl number.

The scaled operating conditions are resumed in Table 2.

The computational domain consists of an upstream plenum characterized by a squared cross section with edge size 67 mm and rounded corners, the primary and secondary radial air swirlers, both characterized by 24 flat vanes with length 6.5 mm and thickness 0.65 mm. The axial thicknesses of the vanes are 6.5 mm for the primary air swirler and 2.6 mm for the secondary air swirler. The geometric areas of the primary and secondary air streams at the entrance of the combustion chamber correspond to 191 mm^2 and 127 mm^2, respectively. The fuel upstream section has a diameter of 11.1 mm while in its downstream section it corresponds to 5.63 mm. The upstream part of the air swirler is axially extended to host the fuel stream with a proper mechanical arrangement. The length of the convergent helical axial swirler in the fuel stream is 17 mm, divided in a 2 mm long straight part, a 10 mm long convergent swirled helix with an axial pitch of 14.5 mm and terminating with a conical shape to limit the extension of a potential recirculation zone downstream the fuel swirler. The cone tip is located 20 mm upstream the entrance of the combustion chamber. The considered thickness for the injector lips separating the three incoming streams corresponds to 0.9 mm, while the thickness of the combustor dome is 3 mm. The dome effusion cooling system is adapted to the new chamber dimension. A total of 244 holes with 0.6 mm diameter is obtained, distributed on seven rings, with a counter-rotating direction with respect to the swirlers.

A compound angle is considered for the three most external rows to provide a better cooling at the flame tube corners as well as for manufacturing reasons. The effusion cooling cylindrical holes per row, the diametral position of the row, as well as the axial and compound angles and the row's air mass flow rate are reported in Table 3. The effusion cooling holes are not explicitly discretized in the numerical geometry, where the coolant injection is realized through numerical patches. A restriction is positioned at the end of the combustion chamber to prevent numerical backflow. Figure 12 shows the considered fluid geometry with the prescribed boundary conditions and the static numerical mesh, that is, constituted by 31 million polyhedral and prismatic cells. A local proximity refinement is applied ensuring at least 26 cells between surface–surface and edge–edge gaps. The explicit sizings imposed for the mesh generation are reported in Table 4.

A reactive LES calculation is used to test the atmospherically scaled geometry, exploiting the pressure-based formulation of ANSYS Fluent 2023 R1. The numerical setup reported in Sec. 3 is retained, with the exception of the mixing and combustion models.

Table 2 Considered operating conditions for the atmospheric scaling at THT-Lab

Quantity	Value	Units	Quantity	Value	Units
W_3^{Lab}	17.038	g s^{-1}	T_3^{Lab}	573	K
$W_{\mathrm{sw}}^{\mathrm{Lab}}$	13.793	g s^{-1}	T_f^{Lab}	300	K
W_f^{Lab}	0.322	g s^{-1}	$\Phi_{\mathrm{sw}}^{\mathrm{Lab}}$	0.80	
$W_{\mathrm{cool}}^{\mathrm{Lab}}$	3.245	g s^{-1}	Φ_3^{Lab}	0.64	

Table 3 Dome cooling parameters

Row	N holes	d (mm)	θ_z (deg)	θ_r (deg)	W (g s^{-1})
1	24	30	20	0	0.319
2	30	38	20	0	0.399
3	36	46	20	0	0.479
4	42	54	20	0	0.559
5	48	62	20	10	0.638
6	44	70	20	25	0.585
7	20	78	20	35	0.266
Total	244	—	—	—	3.245

In this case, the space–time local regularization of the dynamic thickened flame model for large eddy simulations (DTFLES) proposed in Ref. [20] is employed requiring $N = 10$ grid points inside the thickened flame front. The chemical kinetics relies on the skeletal reaction mechanism proposed by Boivin [21] comprising 8 species and 12 reactions, while molecular nitrogen properties are retrieved from the UCSD detailed mechanism [22]. The Colin's formulation [23,24] is chosen as subgrid efficiency model, while the flame sensor is defined according to Ref. [25]

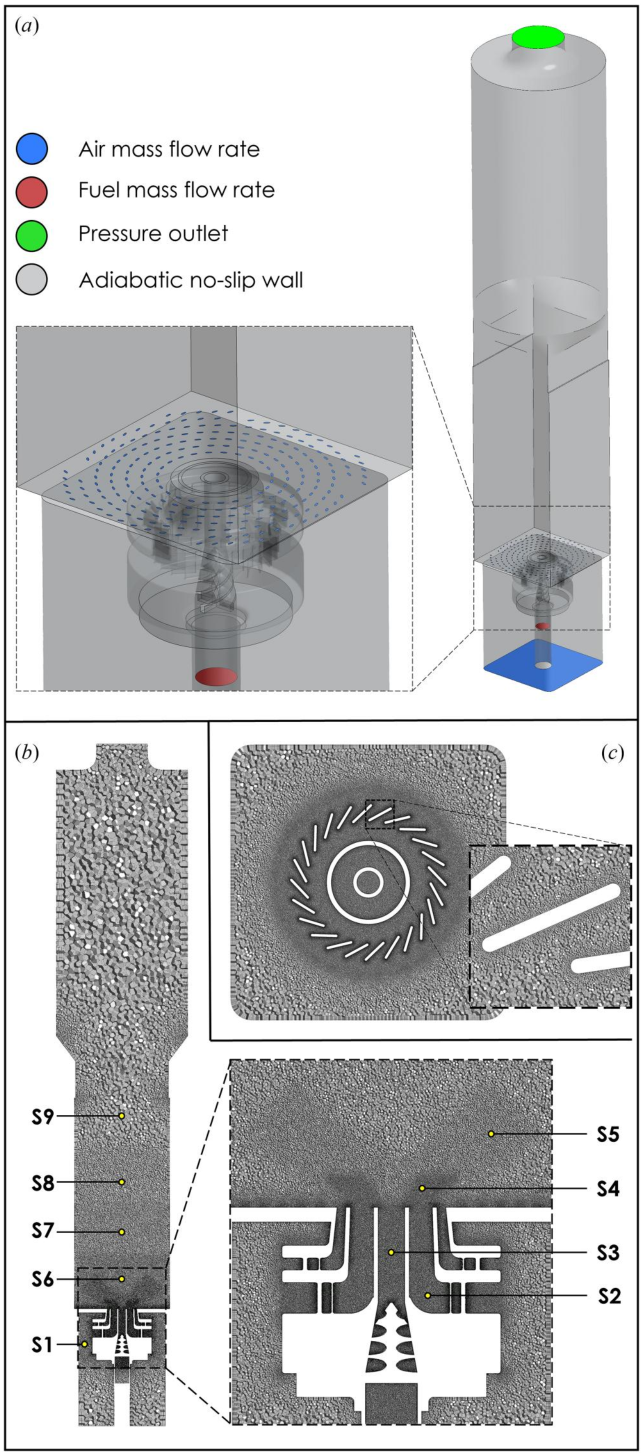

Fig. 12 Computational domain with the assigned boundary conditions (*a*). Polyhedral mesh adopted for the LES calculation and refinement in the swirling ducts region (*b*). Mesh detail on a plane transversal to the secondary air swirler vanes (*c*).

Table 4 Numerical grid sizings

	S1	S2	S3	S4	S5	S6	S7	S8	S9
mm	0.60	0.20	0.20	0.20	0.40	0.65	1.00	1.35	5.00

$$\Omega := \tanh\left(50\,\frac{\overline{|\dot{\omega}|}}{(\max_V \overline{|\dot{\omega}|})}\right) \tag{9}$$

with V is the computational domain and $\overline{|\dot{\omega}|}$ is the spatially filtered absolute value of the third body reaction rate

$$H + O_2\,(+M) \leftrightarrows HO_2\,(+M) \tag{10}$$

A flame index Ψ definition based on the gradients alignment [26] of molecular hydrogen and molecular oxygen mass fractions is chosen as

$$\Psi := \nabla Y_{H_2} \cdot \nabla Y_{O_2} \tag{11}$$

No stretch corrections are considered in this atmospheric study, and the evaluation of the impact of some existing formulations [27,28] could be the object of future investigations. The species laminar diffusion coefficients are calculated with the mixture-averaged diffusion model. The air mass flow rate W_{sw}^{Lab} is prescribed at the upstream plenum inlet patch, while the directed mass flow rates reported in Table 3 are imposed on the different inlet patches of the dome cooling system, for a total coolant mass flow rate given by W_{cool}^{Lab}. The hydrogen mass flow rate W_f^{Lab} is assigned at the inlet patch located upstream the fuel swirler, while atmospheric pressure $P_{atm} = 101325$ Pa is imposed at the outlet section.

The left side of Fig. 13 shows the mean and instantaneous distributions of the axial velocity component on the YZ plane. The extended central recirculation zone is highlighted, together with the external recirculation zone, by null axial velocity isolines. A high-intensity recirculation can be observed around $y \approx 0$ mm, near the exit of the fuel channel. Here, the recirculation zone penetrates few millimeters inside the injector inducing a flow blockage as discussed inRef. [10], spreading radially the hydrogen stream and moving the lips' low-velocity zones inside the primary air channel. A small flow recirculation is again observed at the end of the hydrogen swirler, but with a reduced relative extension with respect to the one observed under high-pressure conditions. The right side of Fig. 13 shows the mean and instantaneous distributions of static temperature on the same YZ plane, and reveals a lifted flame. The outer recirculation zones are characterized by lower temperatures, both time-averaged and instantaneous, and the cold footprints associated with the dome cooling's injections are clearly visible.

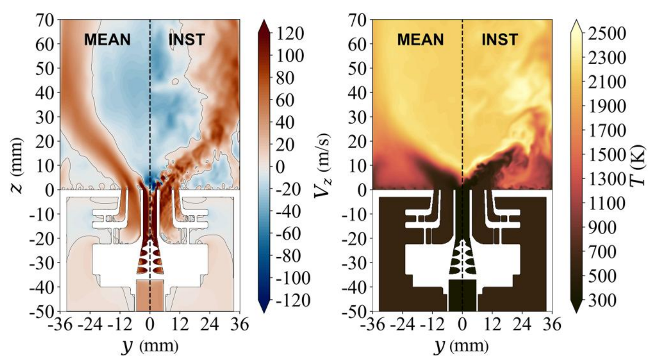

Fig. 13 Mean and instantaneous distributions of axial velocity (left) and static temperature (right) on the *YZ* plane. The solid line highlights the null axial velocity isosurface surrounding the recirculation zones.

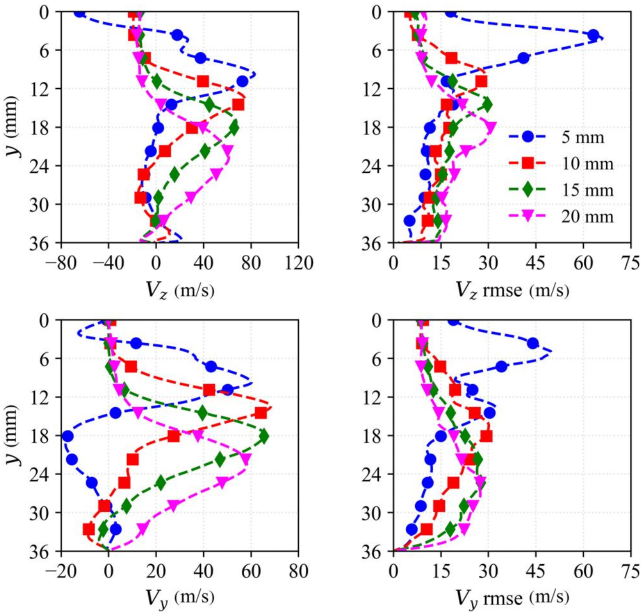

Fig. 14 Mean and rmse velocity profiles at different distances from the dome

The mean and root mean square error (rmse) velocity profiles extracted on the *YZ* plane at different axial locations are reported in Fig. 14. A double peak of axial velocity is reached at $y = 4$ mm and $y = 10$ mm, respectively, in the case of $z = 5$ mm. Moving away from the dome, the second peak progressively shifts radially reducing its intensity, while the first peak completely disappears. The high-intensity recirculation at the exit of the hydrogen stream is clearly visible at $z = 5$ mm where a negative axial velocity is observed at low y coordinates. At high y coordinates, the axial velocity remains positive at $z = 5$ mm and $z = 10$ mm before approaching zero near the wall due to the no-slip condition. Conversely, the axial velocity at $z = 15$ mm and $z = 20$ mm switches from positive to negative values at $y = 30$ mm and $y = 33$ mm, respectively, because of the presence of a lateral recirculation zone visible in Fig. 13. The axial velocity fluctuations show a similar trend with respect to the time-averaged component. Indeed, they are characterized by a peak at low y coordinates that progressively shifts radially when moving away from the dome, but maintaining the same intensity for $z \geq 10$ mm. The strong intensity of the peak at $z = 5$ mm is located at the same y coordinate of the first peak of the time-averaged component. This information, together with the decay of the first peak of axial velocity at higher z values, indicates that is a consequence of the strong acceleration of the hydrogen stream induced by the central recirculation zone.

The radial velocity distribution at $z = 5$ mm shows a local minimum at $y = 2$ mm, a global maximum at $z = 10$ mm and a global minimum at $y = 20$ mm. A nonmonotonic increase is present between the local minimum and the global maximum, where at $y = 5$ mm a small plateau is observed as a consequence of the sum of the blocked hydrogen stream and the flow radial acceleration. At higher z coordinates, the peak of radial velocity is radially shifted and its intensity is first increased up to $z = 10$ mm, before starting decreasing at higher axial coordinates. A similar behavior between the radial velocity profiles at $z \geq 10$ mm is observed for $y < 3$ mm. At high y coordinates, the radial velocity profiles at $z = 10$ mm and $z = 15$ mm assume negative values before approaching the no-slip condition, while the opposite happens at $z = 5$ mm and $z = 20$ mm, due to the shape of the external recirculation zone. The radial velocity fluctuations at $z =$ 5 mm show a triple peak distribution with a global maximum reached at $y = 5$ mm. At higher axial coordinates, the radial velocity fluctuations profiles show similar behaviors with a global maximum reached at progressively increasing radial coordinates, before vanishing approaching the liner's wall. The burner's percentage pressure drop and swirl numbers are numerically evaluated as $(\Delta P/P)^{\mathrm{Lab}} = 5\%$, $S_{\mathrm{H_2}}^{\mathrm{Lab}} = 0.57$, $S_1^{\mathrm{Lab}} = 0.69$, and $S_2^{\mathrm{Lab}} = 1.04$.

The heat release rate is reported in Fig. 15. The left side of the figure shows the mean and instantaneous distributions on the *YZ* plane where a V-shaped flame, stabilizing lifted above the injector, can be observed. The maximum values of heat release rate are assumed along a first flame front and are concentrated around the stoichiometric isoline, as highlighted on the right side of the figure, where the distribution of equivalence ratio is reported together with the instantaneous heat release rate. The central region of this primary flame front burns in very rich conditions above the injector, at the minimum axial coordinate ensuring sufficient mixture reactivity to burn, due to the presence of the highly-intense recirculation zone pushing upstream the reacting mixture. A secondary flame front is present downstream the first one, concentrated around the stoichiometric isoline.

Finally, the mean and instantaneous gas temperature distributions on the dome surface are shown in Fig. 16, revealing a central hotter region that is locally interested by hot recirculating gas pockets. The temperature distribution progressively decreases in radial direction, with the corners of the combustion chamber showing a lower mean and instantaneous gas temperature with respect to the rest of the dome surface, even without a dense distribution of effusion cooling holes in this region.

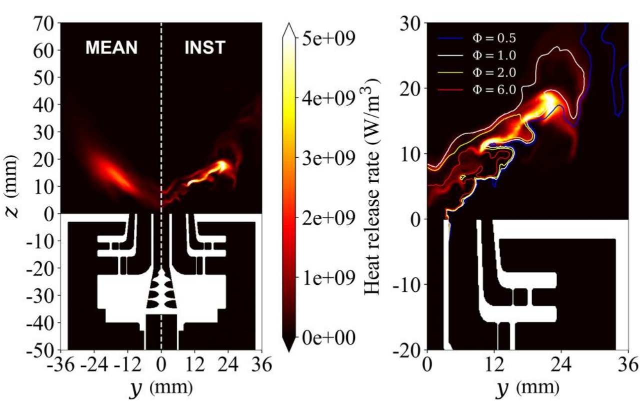

Fig. 15 Mean and instantaneous distributions of heat release rate on the *YZ* plane (left). Superposition of equivalence ratio isolines on the instantaneous heat release rate distribution (right).

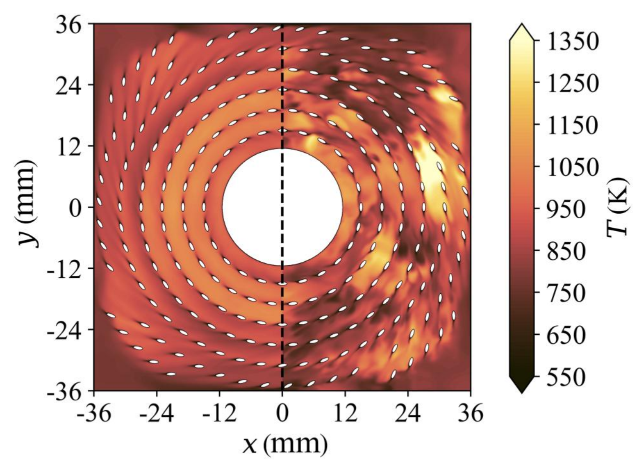

Fig. 16 Mean (left) and instantaneous (right) distributions of gas temperature on the dome surface

5 Conclusion

The numerical design of a novel nonpremixed swirl-stabilized lean 100% hydrogen burner for aero engine applications is carried out. The flame stabilization is achieved using an innovative coaxial triple swirler injector. The design process is conducted under representative engine conditions, and it is adaptable to different thermodynamic cycles. The workflow is divided into multiple stages, involving numerical simulations with progressively increasing levels of detail. Initially, a design space exploration is conducted on a simplified parametric geometry. A promising design point is down-selected from this analysis and further refined in the subsequent stages. The geometrical parameters characterizing the three swirlers are calibrated to achieve the target pressure drop across the burner and the desired swirl numbers. Effusion cooling is incorporated on the dome surface, completing the design. The final burner geometry is tested with a reactive LES calculation under representative engine conditions, revealing a flame that stabilizes anchored to the injector.

The burner is then geometrically scaled to adapt to the reactive test rig installed at the THT-Lab of the University of Florence, and new operating conditions are obtained scaling the reference thermodynamic cycle to the ambient pressure conditions achievable in the test rig. A new solution for the effusion cooling is numerically implemented adapting to the different shape of the combustion chamber. Finally, a detailed reactive LES calculation of the scaled burner under atmospheric pressure conditions demonstrates a V-shaped flame stabilizing lifted above the injector.

Acknowledgment

The authors would like to acknowledge Ignazio Vitale and Fabio Turrini from GE Avio S.r.l. for their precious support.

Funding Data

- The European Union Horizon Europe research and Innovation program under HESTIA (Research Executive Agency Grant Agreement No. 101056865; Funder ID: 10.13039/501100000783).

Data Availability Statement

The authors attest that all data for this study are included in the paper.

Nomenclature

$\hat{\mathbf{e}}$ = unitary basis vector
$\hat{\mathbf{n}}$ = normal unitary vector
P = pressure (Pa)
Q = quadratic scaling factor
r = radius (m)
R = area ratio
s = flame speed (m s^{-1})
S = swirl number
T = temperature (K)
V = velocity component (m s^{-1})
W = mass flow rate (kg s^{-1})

Greek Symbols

α = vane's angle (deg)
γ = injections' tangential angle (deg)
δ = flame thickness (m)
ΔP = pressure drop (Pa)
θ = coolant's injection angle (deg)
ρ = density (kg m^{-3})
Φ = equivalence ratio

Superscripts and Subscripts

cool = coolant air
eff = effective
f = fuel
geo = geometric
H_2 = hydrogen
L = laminar
Lab = lab-scale
r = radial
ref = reference
sw = swirlers
z = axial
ϕ = tangential
1 = primary air swirler
2 = secondary air swirler
3 = upstream the burner

References

[1] Manigandan, S., Praveenkumar, T. R., Ir Ryu, J., Nath Verma, T., and Pugazhendhi, A., 2023, "Role of Hydrogen on Aviation Sector: A Review on Hydrogen Storage, Fuel Flexibility, Flame Stability, and Emissions Reduction on Gas Turbines Engines," Fuel, **352**, p. 129064.
[2] Ajanovic, A., Sayer, M., and Haas, R., 2022, "The Economics and the Environmental Benignity of Different Colors of Hydrogen," Int. J. Hydrogen Energy, **47**(57), pp. 24136–24154.
[3] Gazzani, M., Chiesa, P., Martelli, E., Sigali, S., and Brunetti, I., 2014, "Using Hydrogen as Gas Turbine Fuel: Premixed Versus Diffusive Flame Combustors," ASME J. Eng. Gas Turbines Power, **136**(5), p. 051504.
[4] European Commission, 2023, "Hydrogen Demonstrator for Aviation, HYDEA," European Commission, accessed Dec. 2, 2024, https://cordis.europa.eu/project/id/101102019
[5] European Commission, 2022, "Hydrogen Combustion in Aero Engines, HESTIA," European Commission, accessed Dec. 2, 2024, https://cordis.europa.eu/project/id/101056865
[6] Chen, R. H., and Driscoll, J. F., 1989, "The Role of the Recirculation Vortex in Improving Fuel-Air Mixing Within Swirling Flames," Symp. (Int.) Combust., **22**(1), pp. 531–540.
[7] Goodwin, D. G., Moffat, H. K., Schoegl, I., Speth, R. L., and Weber, B. W., 2023, "Cantera: An Object-Oriented Software Toolkit for Chemical Kinetics, Thermodynamics, and Transport Processes Version 2.6.0," Cantera, accessed Dec. 6, 2024, https://www.cantera.org
[8] O'Conaire, M., Curran, H. J., Simmie, J. M., Pitz, W. J., and Westbrook, C. K., 2004, "A Comprehensive Modeling Study of Hydrogen Oxidation," Int. J. Chem. Kinet., **36**(11), pp. 603–622.
[9] Vilespy, M., Marragou, S., Magnes, H., Aniello, A., Selle, L., Poinsot, T., and Schuller, T., 2023, "Measurements Dataset of Hydrogen/Air Flames in a Dual Swirl Coaxial Injector," TNF Workshop, Toulouse, France, https://tnfworkshop.org/hylon-hydrogen-air-flames-in-a-dual-swirl-coaxial-injector-imft-toulouse/
[10] Degeneve, A., Vicquelin, R., Mirat, C., Caudal, J., and Schuller, T., 2021, "Impact of Co- and Counter-Swirl on Flow Recirculation and Liftoff of Non-Premixed Oxy-Flames Above Coaxial Injectors," Proc. Combust. Inst., **38**(4), pp. 5501–5508.
[11] van Oijen, J., and de Goey, L., 2000, "Modelling of Premixed Laminar Flames Using Flamelet-Generated Manifolds," Combust. Sci. Technol., **161**(1), pp. 113–137.
[12] Marragou, S., Magnes, H., Aniello, A., Selle, L., Poinsot, T., and Schuller, T., 2023, "Experimental Analysis and Theoretical Lift-Off Criterion for H2/Air Flames Stabilized on a Dual Swirl Injector," Proc. Combust. Inst., **39**(4), pp. 4345–4354.
[13] Marragou, S., Magnes, H., Aniello, A., Guiberti, T. F., Selle, L., Poinsot, T., and Schuller, T., 2023, "Modeling of H2/Air Flame Stabilization Regime Above Coaxial Dual Swirl Injectors," Combust. Flame, **255**, p. 112908.
[14] Smagorinsky, J., 1963, "General Circulation Experiments With the Primitive Equations: I. The Basic Experiment," Mon. Weather Rev., **91**(3), pp. 99–164.
[15] Germano, M., Piomelli, U., Moin, P., and Cabot, W. H., 1991, "A Dynamic Subgrid-Scale Eddy Viscosity Model," Phys. Fluids A, **3**(7), pp. 1760–1765.
[16] Lilly, D. K., 1992, "A Proposed Modification of the Germano Subgrid-Scale Closure Method," Phys. Fluids A, **4**(3), pp. 633–635.
[17] Klarmann, N., Sattelmayer, T., Geng, W., and Magni, F., 2016, "Flamelet Generated Manifolds for Partially Premixed, Highly Stretched and Non-Adiabatic Combustion in Gas Turbines," AIAA Paper No. 2016-2120.
[18] Langone, L., Sedlmaier, J., Nassini, P. C., Mazzei, L., Harth, S., and Andreini, A., 2020, "Numerical Modeling of Gaseous Partially Premixed Low-Swirl Lifted Flame at Elevated Pressure," ASME Paper No. GT2020-16305.
[19] Marragou, S., 2023, "Flow Structure, Mixing, Flame Stabilization and Pollutant Emissions From a Coaxial Dual Swirl CH4/H2/Air Injector," Ph.D. thesis, Université de Toulouse, Toulouse, France.
[20] Ballotti, A., Castellani, S., and Andreini, A., 2024, "A Dynamic Thickening Strategy for High-Fidelity Computational Fluid Dynamics Analyses of Multi-Regime Combustion," ASME J. Eng. Gas Turbines Power, **146**(12), p. 121010.
[21] Boivin, P., 2011, "Reduced-Kinetic Mechanisms for Hydrogen and Syngas Combustion Including Autoignition," Ph.D. thesis, DEPARTAMENTO DE INGENIERÍA TÉRMICA Y DE FLUIDOS Escuela Politécnica Superior, Universidad Carlos III de Madrid, Madrid, Spain.
[22] Mechanical and Aerospace Engineering (Combustion Research), 2012, "Chemical-Kinetic Mechanisms for Combustion Applications," University of California, San Diego, CA, http://web.eng.ucsd.edu

[23] Colin, O., Ducros, F., Veynante, D., and Poinsot, T., 2000, "A Thickened Flame Model for Large Eddy Simulations of Turbulent Premixed Combustion," Phys. Fluids, **12**(7), pp. 1843–1863.
[24] Durand, L., and Polifke, W., 2007, "Implementation of the Thickened Flame Model for Large Eddy Simulation of Turbulent Premixed Combustion in a Commercial Solver," ASME Paper No. GT2007-28188.
[25] Legier, J. P., Poinsot, T., and Veynante, D., 2000, "Dynamically Thickened Flame LES Model for Premixed and Non-Premixed Turbulent Combustion," Proceedings of the Summer Program, Vol. 12 Center for Turbulence Research, Stanford, CA, pp. 157–168.
[26] Yamashita, H., Shimada, M., and Takeno, T., 1996, "A Numerical Study on Flame Stability at the Transition Point of Jet Diffusion Flames," Symp. (Int.) Combust., **26**(1), pp. 27–34.
[27] Detomaso, N., Hok, J. J., Dounia, O., Laera, D., and Poinsot, T., 2023, "A Generalization of the Thickened Flame Model for Stretched Flames," Combust. Flame, **258**, p. 113080.
[28] Gaucherand, J., Schulze-Netzer, C., Laera, D., and Poinsot, T., 2024, "A Subgrid-Scale Model to Account for Thermo-Diffusive Effects in Artificially Thickened LES Models for Lean Turbulent Premixed Ammonia/Hydrogen Flames," Proc. Combust. Inst., **40**(1–4), p. 105198.